

TSJNet: A Multi-modality Target and Semantic Awareness Joint-driven Image Fusion Network

Yuchan Jie^{a,1}, Yushen Xu^{a,1}, Xiaosong Li^{a,*}, Huafeng Li^b, Haishu Tan^a, Feiping Nie^c

^a*School of Physics and Optoelectronic Engineering, Foshan University, 528225, Foshan, China*

^b*School of Information Engineering and Automation, Kunming University of Science and Technology, 650500, Kunming, China*

^c*School of Artificial Intelligence, Optics and Electronics (iOPEN), School of Computer Science, Northwestern Polytechnical University, Xi'an 710072, China*

Abstract

This study aims to address the problem of incomplete information in unimodal images for semantic segmentation and object detection tasks. Existing multimodal fusion methods suffer from limited capability in discriminative modeling of multi-scale semantic structures and salient target regions, which further restricts the effective fusion of task-related semantic details and target information across modalities. To tackle these challenges, this paper proposes a novel fusion network termed TSJNet, which leverages the semantic information output by high-level tasks in a joint manner to guide the fusion process. Specifically, we design a multi-dimensional feature extraction module with dual parallel branches to capture multi-scale and salient features. Meanwhile, a data-agnostic spatial attention module embedded in the decoder dynamically calibrates attention allocation across different data domains, significantly enhancing the model's generalization ability. To optimize both fusion and advanced visual tasks, we balance performance by combining fusion loss with semantic losses. Additionally, we have developed a multimodal unmanned aerial vehicle (UAV) dataset covering multiple scenarios (UMS). Extensive experiments demonstrate that TSJNet achieves outstanding performance on five public datasets (MSRS, M³FD, RoadScene, LLVIP, and TNO) and our UMS dataset. The generated fusion results exhibit favorable visual effects, and compared to state-of-the-art methods, the mean average precision (mAP@0.5) and mean intersection over union (mIoU) for object detection and segmentation, respectively, improve by 7.97% and 10.88%. The code and the dataset has been publicly released at <https://github.com/XylonXu01/TSJNet>.

Keywords: Multi-modal image fusion, object detection, semantic segmentation, benchmark.

1. Introduction

Multisensor integration is vital for intelligent technologies, such as unmanned aerial vehicle (UAV) precision combat and autonomous driving. As sensor technology advances, leveraging multi-modal images becomes crucial for complex real-world scene analysis. Visible and infrared sensors, commonly employed, exhibit limitations. While visible light sensors struggle to highlight targets effectively under low-light conditions, infrared sensors, unaffected by this issue, provide low scene resolution and capture texture details poorly [1]. Fortunately, multi-modal image fusion (MMIF) can mitigate these challenges by synthesizing data from multiple sources, compensating for information loss in single-modal data, and enhancing understanding and perception for both human and machine vision. Moreover, MMIF is anticipated to yield more accurate representations of targets and scenes, positively impacting downstream tasks such as semantic segmentation and object detection [2, 3].

Recent advancements in deep learning (DL) feature extraction have propelled the development of DL-based MMIF methods. Notably, convolutional neural networks (CNN) [6], generative adversarial networks (GAN) [4],

*Corresponding author

Email addresses: jyc981214@163.com (Yuchan Jie), 2112355010@stu.fosu.edu.cn (Yushen Xu), 1ixiaosong@buaa.edu.cn (Xiaosong Li), hfchina99@163.com (Huafeng Li), tanhaishu@fosu.edu.cn (Haishu Tan), feipingnie@gmail.com (Feiping Nie)

¹Equal Contribution

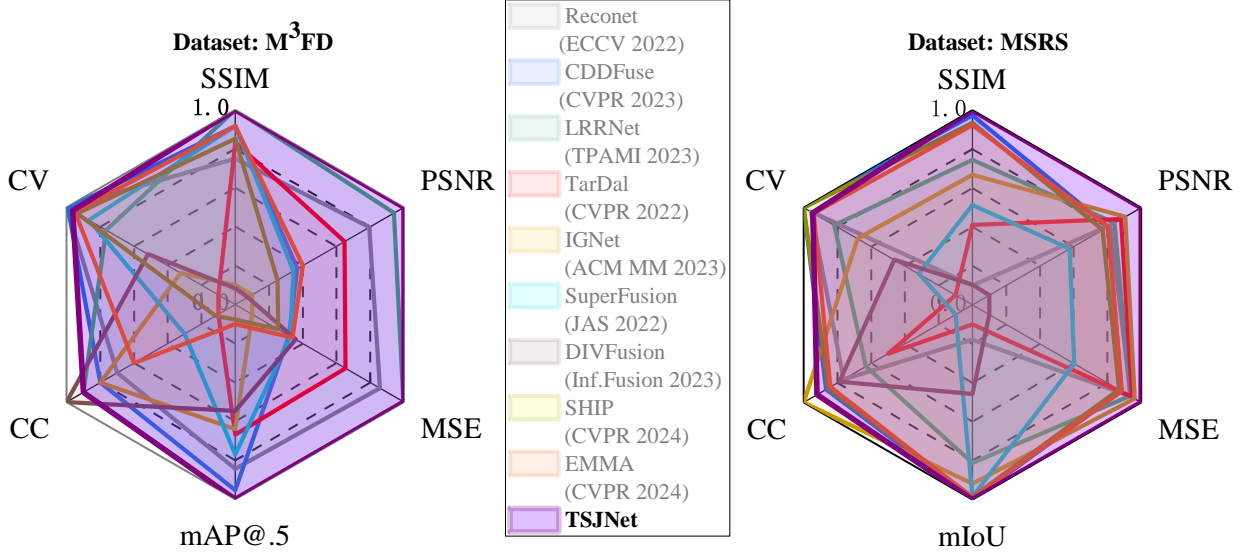


Figure 1: Comparison of results with SOTA methods on the M³FD [4] and MSRS [5] datasets. The radar map highlights the superiority of the TSJNet.

transformer[7], diffusion models [8, 9] and autoencoders (AE) [10, 11] have emerged as key approaches in this field, owing to their robust capabilities in feature representation. However, these approaches encounter two problems. First, existing multimodal fusion methods suffer from deficiencies in multi-scale semantic modeling and salient target feature characterization, which renders them unable to effectively integrate cross-modal semantic details and target information. Second, existing methods overlook the synergistic relationship between fusion tasks and subsequent high-level tasks. Third, existing multimodal image fusion datasets are predominantly derived from ground-level perspectives, lacking multi-scenario and multi-condition samples that cover UAV aerial photography. This deficiency restricts the generalization capability of current methods in complex aerial environments.

To address the first issue, existing fusion models [12, 13, 14] still suffer from deficiencies in multi-scale semantic modeling and salient target feature characterization, which renders them unable to effectively integrate cross-modal task-relevant semantic details and target information. Taking infrared-visible image fusion (IVIF) as a typical example, although the two modalities are captured from the same target scene, their feature representations exhibit substantial discrepancies: the large-scale contours of targets belong to shared features, whereas the thermal radiation information in infrared images and the texture edge information in visible-light images are the salient features specific to each modality, respectively. Despite the Dif-Fusion model [15] integrating infrared and visible-light images into multi-channel inputs and extracting fused features via a diffusion model, it lacks a dedicated mechanism tailored to the disparities between shared and salient features. Consequently, it remains difficult for the model to fully integrate global and local information across multiple modalities. It is thus evident that there is an urgent need for an algorithm capable of simultaneously capturing shared and salient features, as well as achieving effective fusion of multi-scale semantic and target information.

For the second problem, a valuable MMIF model produces high-quality images in real-world scenarios and supports downstream tasks. While some existing methods [16, 17, 18, 19] demonstrate good fusion performance, they often neglect to achieve mutual benefits between downstream tasks and image fusion. For example, CDDFuse [11] incorporates an autoencoder based on Restomer and a feature fusion layer based on Lite Transformer and reversible neural networks. While this approach takes complementary feature extraction into account during the fusion process, it places insufficient emphasis on semantic information. Fortunately, recent studies [20] have established a strong connection between image fusion and object detection or semantic segmentation, though they may not fully explore the deeper correlations among these three aspects.

Additionally, in military security and combat scenarios, aerial imagery presents challenges for drone-based object

detection and semantic segmentation due to complex backgrounds and varying lighting conditions. However, existing MMIF datasets [21, 22, 23, 5, 4] primarily focus on traditional ground-level perspectives, significantly limiting the adaptability of current fusion methods to the diverse environments encountered from a drone’s viewpoint, thereby impacting their effectiveness in practical applications.

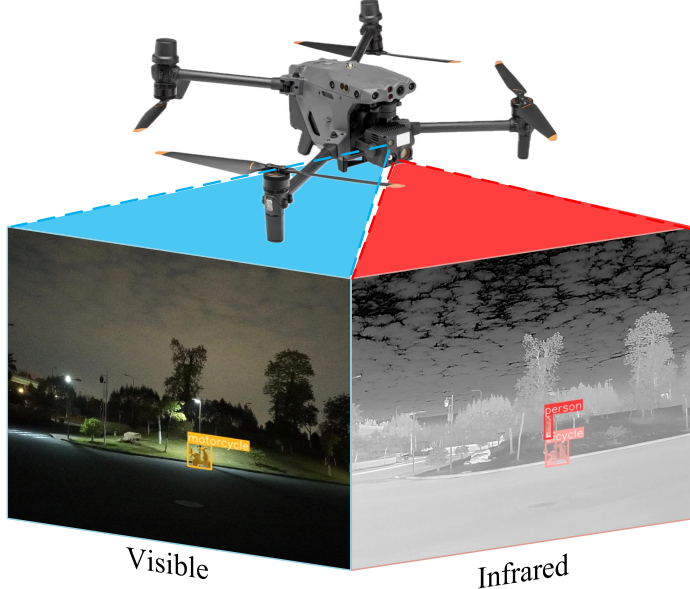


Figure 2: Unmanned Aerial Vehicle Data Acquisition System. The visible and infrared image pairs in the same scene are captured using a UAV equipped with both a zoom camera and an infrared camera.

To address the aforementioned challenges, we propose TSJNet, a multi-feature learning MMIF network designed to effectively integrate multi-scale shared features and salient modality-specific information for downstream segmentation and detection tasks. Specifically, we design a Multi-Dimensional Feature Extraction Module (MDM) with a dual-branch structure that captures complementary multi-scale semantic features and salient modality-specific features, enabling effective integration of cross-modal semantic details and target information. Additionally, we integrate semantic segmentation and object detection networks to guide the refinement of fusion features. This is achieved by combining segmentation and detection losses with the fusion loss, enhancing the accuracy of fusion results in downstream tasks. Fig. 1 demonstrates that the proposed network outperforms nine state-of-the-art (SOTA) methods in fusion performance. Additionally, Fig. 2 illustrates our construction of a new benchmark for the UAV multi-scenario dataset (UMS), encompassing both aerial and conventional viewpoints. Our contributions are as follows:

1. We present TSJNet, an MMIF network that synergistically combines detection and segmentation. TSJNet generates high-quality fusion images and significantly improves the accuracy of unimodal images in object detection and semantic segmentation tasks.
2. We design the MDM with dual parallel branches to capture multi-scale and salient features, facilitating comprehensive cross-modal representation.
3. We create a comprehensive multi-modal UAV dataset consisting of 346 registered image pairs across six diverse scenarios, suitable for image fusion, detection and segmentation tasks.

2. Related work

2.1. Multi-modal image fusion

Over recent years, numerous DL-based MMIF approaches have emerged[24, 25], primarily falling into five categories: CNN- [26], GAN- [27], transformer-[28, 7, 29], diffusion model- [30, 15, 31], and AE-[11, 32, 33, 34] based methods.

Table 1: Comparison of the proposed UMS dataset with five commonly used public multi-modal datasets

Datasets	Image Pairs	Resolution	Camera angle	Poor light	Objects	Annotation
TNO	261	768×576	ground	few	few	×
RoadScene	221	768×576	drive	moderate	moderate	×
LLVIP	16836	1080×720	surveillance	✓	✓	×
MSRS	1444	640×480	drive	moderate	✓	Segmentation
M ³ FD	4200	1024×768	ground, drive	moderate	✓	Detection
UMS	346	640×512	ground, drive, flight	✓	✓	Segmentation, Detection

Despite remarkable progress in DL for low-level vision, driven by the nonlinear fitting power of deep networks, limited attention has been paid to integrating high-level tasks. Cross-task learning offers a way to alleviate data scarcity and the lack of ground truth [35]. Liu et al. [36] designed a dual-task hierarchy to jointly enhance semantic perception and image fusion. To emphasize both target-related information and pixel-level details in an image, Sun et al. [2] leveraged insights from object detection networks to direct MMIF. To explore the potential of image-level fusion in semantically driven methods, Tang et al. [37] introduced a scene-authenticity-constrained image-fusion network with incremental semantic integration. Additionally, Xu et al. [38] leveraged image-fusion responses to enhance registration accuracy. Wang et al. [39] proposed a paradigm for handling misaligned infrared and visible light images using intermodal generation and registration. To overcome limitations of two-stage unregistered IVIF, MulFS-CAP [40] introduced a shared shallow feature encoder with a learnable modality dictionary, enabling consistent feature learning and cross-modality alignment.

2.2. Benchmarks

Existing MMIF datasets often target specific scenarios. For example, the TNO dataset [21] covers 261 pairs of multi-band images from military, rural, and urban scenes. The RoadScene dataset [22] is dedicated to road scenes, containing 221 pairs of registered images. LLVIP [23] predominantly features nighttime urban road scenes with 16836 image pairs. The MSRS dataset [5] specializes in multispectral road scenes and includes 1444 pairs of registered images. The M³FD dataset [4] encompasses various lighting conditions and challenging scenarios, totaling 4200 pairs of registered images. Despite their unique characteristics, these datasets are constrained by specific shooting perspectives and locations, posing challenges in fully capturing the complexity and diversity of MMIF in the real world.

Table 1 summarizes existing public multimodal datasets and the proposed UMS dataset in terms of counts, resolution, perspectives, lighting, objectives, and label availability.

3. The proposed TSJNet

3.1. Problem formulation

Unlike prior image-fusion methods that focus solely on visual effects, our approach aims to generate information-rich images that satisfy the dual perception of segmentation and detection requirements. To achieve this, we unify the three tasks into cohesive objective. For illustrative purposes, consider the case of IVIF, where the infrared, visible, and fused images possess dimensions of $p \times q$. We denote these images as individual vectors $\mathbf{I}, \mathbf{V}, \mathbf{F} \in \mathbb{R}^{p \times q \times l}$, respectively, with l representing the number of channels. The optimization framework is defined as follows:

$$\min_{\omega_F, \omega_d, \omega_s} f_F(\mathbf{F}, \Phi(\mathbf{I}, \mathbf{V}, \omega_F)) + f_d(\mathbf{d}, \Psi(\mathbf{I}, \mathbf{V}, \mathbf{F}, \omega_d)) + f_s(\mathbf{s}, \varphi(\mathbf{F}, \omega_s)) \quad (1)$$

where $f(\cdot)$ denotes the fidelity term. \mathbf{F} , \mathbf{d} , and \mathbf{s} represent the fusion, detection, and segmentation results, respectively. These are produced by the fusion network Φ , detection network Ψ and segmentation network φ , with adjustable parameters denoted as $\omega_F, \omega_d, \omega_s$.

Fig. 3 illustrates the gradient optimization process for fusion, detection, and segmentation, where the joint loss function balances these components to achieve the global optimal solution. Specifically, we adopt DeepLabV3+ with ResNet101 [41] and Faster R-CNN [42] as the baseline models for detection and segmentation, providing both target and semantic information.

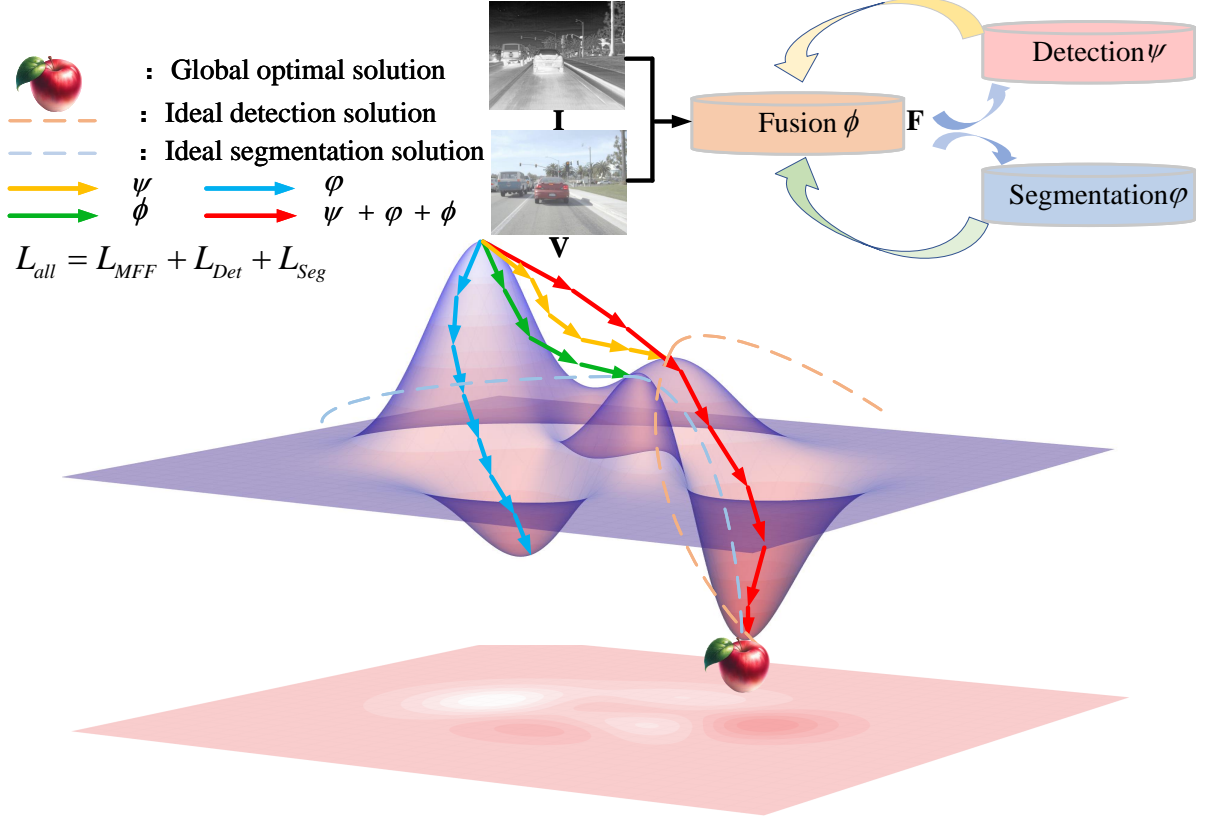


Figure 3: Fusion gradient optimization process. The joint loss design of fusion, detection, and segmentation optimizes the balance among the fusion, detection, and segmentation solutions to achieve the optimal global solution.

3.2. Details of TSJNet

Fig. 5 illustrates the detailed TSJNet model. We introduce symbols to enhance formulation clarity. The paired input images—specifically the infrared and visible images—are denoted as $\mathbf{I} \in \mathbb{R}^{p \times q}$ and $\mathbf{V} \in \mathbb{R}^{p \times q \times 3}$, respectively.

3.2.1. Base ResNeSt Encoder (BRE)

The encoder is comprised two components: a ResNeSt [43] block and a convolutional layer-based feature refinement block. The *BRE* extracts hierarchical features $\mathbf{F}_I^B, \mathbf{F}_V^B$ from \mathbf{I}, \mathbf{V} , that is,

$$\mathbf{F}_I^B = BRE(\mathbf{I}), \quad \mathbf{F}_V^B = BRE(\mathbf{V}) \quad (2)$$

The split-attention of ResNeSt combines channel attention mechanisms with a multi-path network architecture, effectively capturing cross-channel feature correlations. Thus, we integrate ResNeSt into the encoder to learn rich and diverse feature representations of multi-modal images, further enhancing image content understanding.

3.2.2. MDM based fusion layer

To extract and integrate multi-scale shared semantic features and salient modality-specific features from multi-modal images, we propose the MDM. This dual-branch feature extraction unit consists of a Neighborhood Attention Transformer (NAT) [44] branch and a Main Feature Module (MFM). As illustrated in Fig. 4, the NAT branch employs a hierarchical structure by stacking NAT blocks to model multi-scale contextual information, effectively capturing both local and global dependencies. In our implementation, the NAT is configured with a neighborhood size of

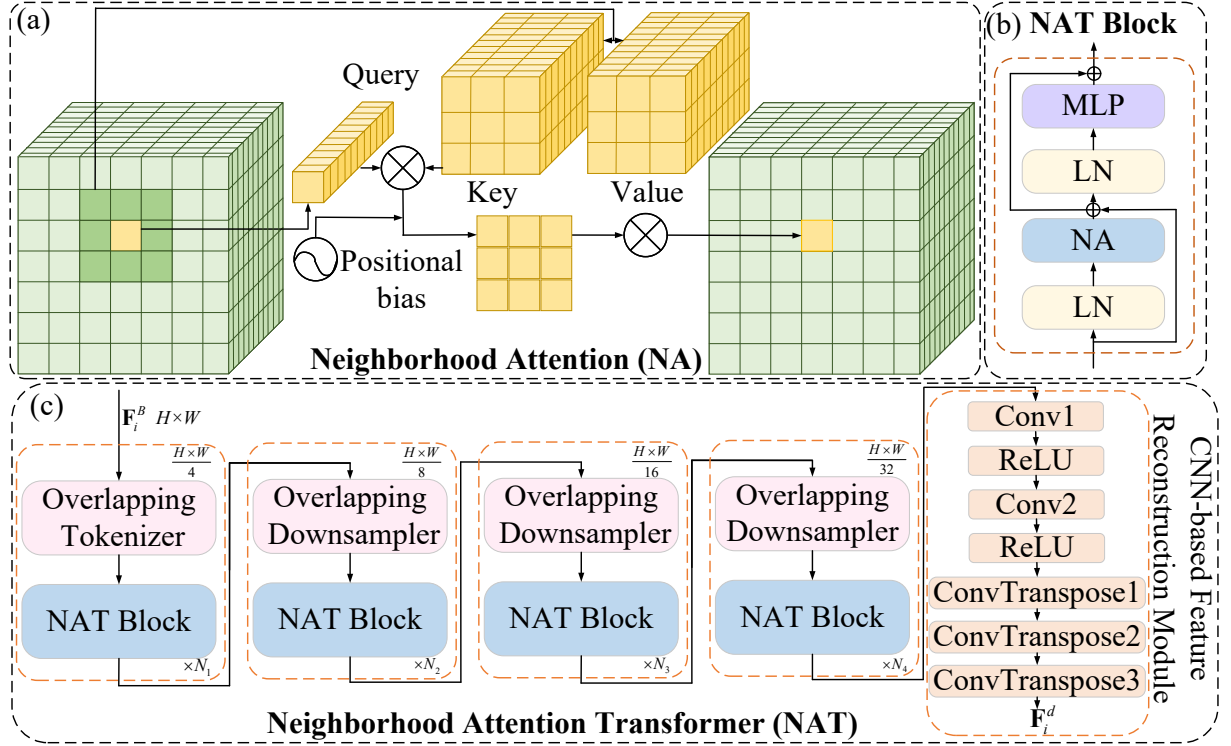


Figure 4: The structure of neighborhood attention transformer.

7×7 following the default design, balancing receptive field coverage and computational efficiency. Additionally, an overlapping tokenizer is introduced to enhance spatial coherence and local continuity of feature embeddings by incorporating overlapping receptive fields during tokenization.

The MFM branch incorporates pooling operations, global feature representations, and a saliency enhancement mechanism. Additionally, the introduction of a residual subnetwork preserves modality-specific attributes, preventing the loss of significant information. As shown in Fig. 5 (c), \mathbf{F}_c is generated through a convolutional layer and is processed by residual and salient feature extraction branches. The salient feature extraction branch performs average pooling and max pooling for contour and texture information extraction from the background. Dual pooling is followed by global average pooling to extend further image feature representation. Subsequently, the weights for different channels are computed using two fully connected layers and a sigmoid layer, enhancing significant feature descriptions. Summing this branch with a residual branch extracts salient and background information from infrared and visible images. The expressions are as follows:

$$\{\mathbf{F}_i^d, \mathbf{F}_i^n\} = MDM(\mathbf{F}_i^B), \quad \{\mathbf{F}_v^d, \mathbf{F}_v^n\} = MDM(\mathbf{F}_v^B) \quad (3)$$

where \mathbf{F}_i^d and \mathbf{F}_i^n represent the salient features of the background and target in \mathbf{I} . \mathbf{F}_v^d and \mathbf{F}_v^n are for \mathbf{V} .

By aggregating salient background and target features from \mathbf{I} and \mathbf{V} , and subsequently inputting them into the MFM and NAT for global-local, shared-special feature extraction, we acquire the pre-fused background and target features, denoted as \mathbf{F}_d and \mathbf{F}_n .

$$\mathbf{F}_d = MFM(\mathbf{F}_i^d + \mathbf{F}_v^d), \quad \mathbf{F}_n = NAT(\mathbf{F}_i^n + \mathbf{F}_v^n) \quad (4)$$

3.2.3. Base ResNeSt Decoder (BRD)

The design of BRD aligns with the structure of BRE while enhancing the overall stability and robustness of the model. Unlike BRE, BRD incorporates the Dataset-Agnostic Spatial Attention Layer (SA) [45]. The SA module effectively allocates cross-modal spatial attention weights, enabling the localization of crucial features in the source

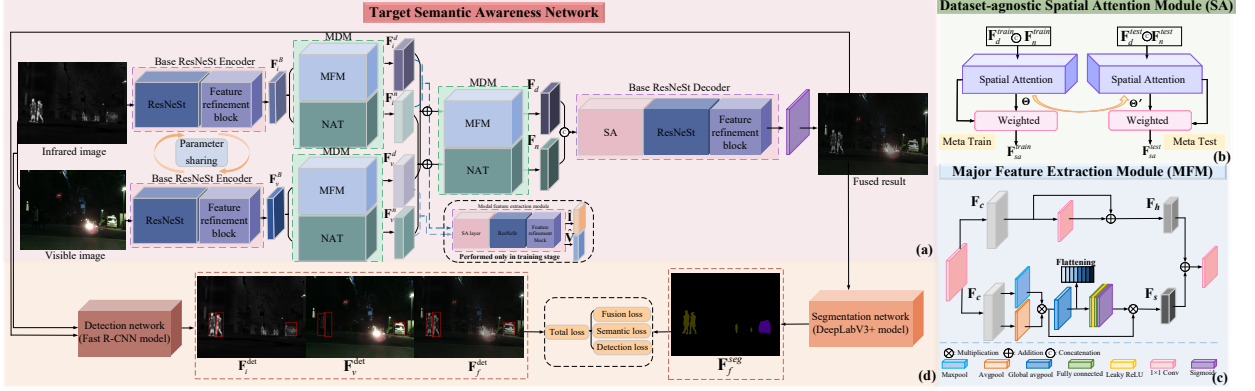


Figure 5: Framework of the proposed TSJNet with dual drivers of segmentation and detection. Our model comprises a base ResNeSt encoder, a dual-branch fusion layer, and a base ResNeSt decoder. The MDM module integrates two parallel branches: NAT, which captures multi-scale contextual dependencies through localized attention and hierarchical design, and MFM, which focuses on extracting salient structures via residual and saliency-enhanced representations.

images across diverse datasets. This attention mechanism facilitates efficient information interaction between multi-modal images, ensuring that the most relevant regions, such as target objects or pathological features, are emphasized for accurate fusion. By highlighting significant areas while maintaining a balanced attention distribution, SA enhances the complementarity and discriminative power of the fused features, reducing redundancy in the model’s information processing. Furthermore, the SA module helps preserve both local details and structural attributes in the fused image, significantly improving the model’s generalization ability and performance in downstream tasks, such as object detection and semantic segmentation. During training, SA allows for effective feature interaction and ensures robust performance across various datasets. The pre-fused complementary information extracted by the fusion layer is subsequently used as input to $BRD(\cdot)$ or image reconstruction, resulting in a high-quality fused output \mathbf{F} , which is expressed as follows:

$$\mathbf{F}, \mathbf{att} = BRD(\mathbf{F}_d + \mathbf{F}_n) \quad (5)$$

where \mathbf{att} is the attention weight matrix generated in the decoder training phase.

3.3. Loss function

TSJNet not only enhances the fusion performance but also improves the accuracy of fused images in higher-level tasks by embedding object position and pixel category information into the fusion feature extraction process. Specifically, we combine the detection \mathcal{L}_{Det} and segmentation losses \mathcal{L}_{Seg} with multifaceted fusion loss \mathcal{L}_{MFF} . The detection loss is introduced following the formulation in [42], while the segmentation loss employs a cross-entropy function. The precise formulation of the fusion loss can be presented as:

$$\mathcal{L}_{\text{all}} = \mathcal{L}_{\text{MFF}} + \mathcal{L}_{\text{Det}} + \mathcal{L}_{\text{Seg}} \quad (6)$$

where \mathcal{L}_{all} denotes the total loss.

3.3.1. MultiFacet Fusion Loss

The quality of fused images directly impacts the accuracy of advanced tasks. In object detection, precise localization and recognition rely on the complete preservation of object edges and feature information. For semantic segmentation, pixel-level classification requires rich visual details and background information. Accordingly, MF-FLoss optimizes fused images to further enhance the overall performance of detection and segmentation tasks.

\mathcal{L}_{MFF} prioritizes preserving target texture, edge information, and background continuity via the loss of the structural similarity metric, $\mathcal{L}_{\text{ssim}}$, which is critical for pixel-level classification in semantic segmentation, as expressed in Eq.7.

$$\mathcal{L}_{\text{ssim}} = \frac{1}{2} (1 - \text{ssim}(\mathbf{F}, \mathbf{I})) + \frac{1}{2} (1 - \text{ssim}(\mathbf{F}, \mathbf{V})) \quad (7)$$

where $\text{ssim}(\cdot)$ calculates the structural similarity.

To enhance the generalization of the fusion model and improve its capability in optimizing multi-modal image features, we introduce the diversity loss \mathcal{L}_{div} [45]. Specifically, \mathcal{L}_{div} imposes constraints on the attention weight matrix of SA, ensuring the fusion model focuses more effectively on the critical regions within the multi-modal image, as expressed in Eq.8.

$$\mathcal{L}_{\text{div}} = -\frac{1}{m} \sum_{i=1}^m \left(1 - \max_j \mathbf{att}_{i,j} \right) + \frac{1}{mn} \sum_{i=1}^m \sum_{j=1}^n \mathbf{att}_{i,j} \quad (8)$$

where m and n are the number of rows and columns, respectively.

In summary, the objective of our model can be succinctly summarized as follows:

$$\mathcal{L}_{\text{MFF}} = \alpha_1 \mathcal{L}_{\text{div}} + \mathcal{L}_{\text{ssim}} + \alpha_2 \mathcal{L}'_{\text{mse}} + \alpha_3 \mathcal{L}''_{\text{mse}} \quad (9)$$

where $\mathcal{L}'_{\text{mse}} = \|\mathbf{I} - \hat{\mathbf{I}}\|_2^2$ and $\mathcal{L}''_{\text{mse}} = \|\mathbf{V} - \hat{\mathbf{V}}\|_2^2$, $\hat{\mathbf{I}}$ and $\hat{\mathbf{V}}$ are outputs of BRD. α_1 , α_2 , and α_3 are the tuning parameters.

3.3.2. Detection Loss

The infrared, visible, and fused results independently feed into the detection network for detection loss computation. We represent the detection loss for the \mathbf{I} , \mathbf{V} , and \mathbf{F} as $\mathcal{L}_{\text{det}}^I$, $\mathcal{L}_{\text{det}}^V$, and $\mathcal{L}_{\text{det}}^F$, respectively. The detection loss \mathcal{L}_{Det} can be denoted as follows,

$$\mathcal{L}_{\text{Det}} = \mathcal{L}_{\text{det}}^I + \mathcal{L}_{\text{det}}^V + \mathcal{L}_{\text{det}}^F \quad (10)$$

To enhance computational efficiency of our model, we eliminated the classification loss from the original object detection loss [42], retaining solely the regression loss [2]. Furthermore, the detection loss function works only when the fusion network needs to be modified. Consider a fusion-detection network, where example,

$$\mathcal{L}_{\text{det}}^F(u, t^u, v) = [u \geq 1] \mathcal{L}_{\text{det}}^F(t^u, v) \quad (11)$$

where u is the ground truth class, t^u is the the predicted outcome of the bounding box, and v is the regression goal of the ground truth bounding box. The Iverson bracket indicator function $[u \geq 1]$ is 1 when $u \geq 1$ is satisfied, and 0 otherwise. We label the background class as $u = 0$.

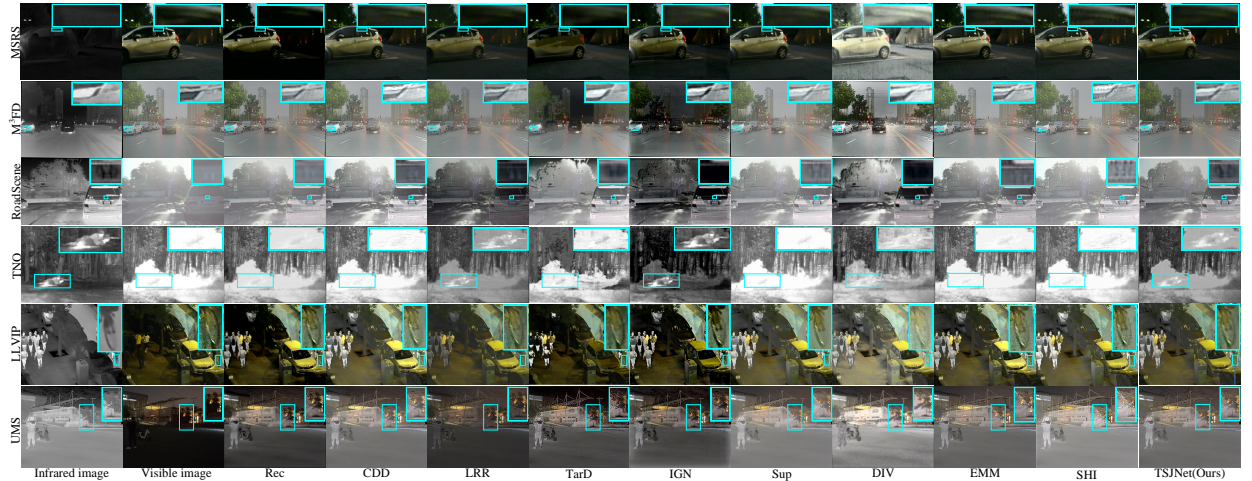


Figure 6: Subjective comparisons of different methods on MSRS, M³FD, RoadScene, LLVIP, TNO, and UMS datasets.

Table 2: Objective comparisons of different methods on MSRS, M³FD, RoadScene, LLVIP, TNO, and the proposed UMS datasets. The top three values are marked in red, green, and blue.

MSRS [5] dataset							M ³ FD [4] dataset						
Method	SSIM↑	PSNR↑	MSE↓	VIF↑	CC↑	CV↓	Method	SSIM↑	PSNR↑	MSE↓	VIF↑	CC↑	CV↓
ReC [46]	0.30	16.38	2005.55	0.31	0.56	319.06	ReC [46]	0.67	14.11	2989.60	0.33	0.51	496.54
CDD [11]	0.68	16.23	2437.54	0.44	0.60	230.35	CDD [11]	0.69	13.04	4035.47	0.37	0.52	501.84
LRR [10]	0.59	16.61	2039.84	0.33	0.51	613.42	LRR [10]	0.70	14.48	2722.86	0.36	0.53	678.53
TarD [4]	0.46	16.99	1941.00	0.34	0.46	2342.74	TarD [4]	0.68	13.74	3385.62	0.39	0.44	1271.50
IGN [16]	0.56	17.22	1811.24	0.32	0.65	903.80	IGN [16]	0.58	12.11	4649.93	0.24	0.52	1020.07
Sup [47]	0.50	14.05	4717.51	0.24	0.27	1667.85	Sup [47]	0.69	12.98	4019.42	0.40	0.47	598.91
DIV [48]	0.34	8.51	9613.72	0.18	0.57	1364.19	DIV [48]	0.59	12.30	3957.61	0.23	0.54	871.24
EMM [49]	0.66	16.24	2441.76	0.39	0.59	354.38	EMM [49]	0.69	13.12	3994.92	0.33	0.50	525.45
SHI [50]	0.66	15.93	2560.61	0.40	0.59	350.71	SHI [50]	0.68	12.74	4155.72	0.35	0.45	546.44
TSJNet	0.69	18.13	1502.60	0.45	0.62	344.20	TSJNet	0.70	14.63	2714.86	0.33	0.53	524.41
RoadScene [22] dataset							LLVIP [23] dataset						
Method	SSIM↑	PSNR↑	MSE↓	VIF↑	CC↑	CV↓	Method	SSIM↑	PSNR↑	MSE↓	VIF↑	CC↑	CV↓
ReC [46]	0.72	15.40	2404.92	0.32	0.62	460.00	ReC [46]	0.42	14.64	2281.86	0.30	0.69	302.05
CDD [11]	0.67	14.03	3077.02	0.25	0.63	426.30	CDD [11]	0.64	14.58	2315.02	0.41	0.68	332.29
LRR [10]	0.58	11.82	4401.71	0.24	0.62	629.70	LRR [10]	0.59	15.93	1688.62	0.39	0.68	580.90
TarD [4]	0.69	14.82	2603.71	0.31	0.58	1255.83	TarD [4]	0.56	14.33	2508.97	0.41	0.65	1095.24
IGN [16]	0.52	10.31	6693.45	0.28	0.60	1033.15	IGN [16]	0.55	14.97	2137.50	0.24	0.68	638.59
Sup [47]	0.74	14.51	2928.35	0.34	0.60	420.00	Sup [47]	0.64	14.62	2306.66	0.38	0.68	360.89
DIV [48]	0.61	13.86	3033.92	0.19	0.62	907.78	DIV [48]	0.46	10.44	6362.27	0.25	0.68	645.38
EMM [49]	0.66	14.04	3037.58	0.25	0.62	416.33	EMM [49]	0.64	14.59	2320.60	0.35	0.68	310.12
SHI [50]	0.66	13.78	3364.21	0.27	0.57	425.21	SHI [50]	0.62	13.94	2697.28	0.35	0.66	374.81
TSJNet	0.70	14.52	2544.58	0.33	0.64	516.82	TSJNet	0.64	15.97	1697.69	0.37	0.67	457.46
TNO [21] dataset							UMS dataset						
Method	SSIM↑	PSNR↑	MSE↓	VIF↑	CC↑	CV↓	Method	SSIM↑	PSNR↑	MSE↓	VIF↑	CC↑	CV↓
ReC [46]	0.73	17.67	1598.49	0.36	0.60	337.37	ReC [46]	0.61	13.95	2730.45	0.31	0.58	545.29
CDD [11]	0.67	14.88	2631.73	0.30	0.61	276.78	CDD [11]	0.65	12.59	3753.37	0.34	0.58	397.27
LRR [10]	0.64	14.42	2895.15	0.27	0.57	501.70	LRR [10]	0.60	13.84	2912.62	0.23	0.57	1051.11
TarD [4]	0.73	17.32	1861.51	0.37	0.57	594.18	TarD [4]	0.40	12.09	4128.53	0.14	0.47	666.21
IGN [16]	0.44	11.45	5656.93	0.15	0.30	1146.83	IGN [16]	0.56	13.10	3297.93	0.24	0.55	371.82
Sup [47]	0.75	16.46	2143.23	0.39	0.59	287.04	Sup [47]	0.65	12.80	3691.07	0.35	0.52	436.49
DIV [48]	0.58	13.05	3401.38	0.22	0.61	596.28	DIV [48]	0.59	11.92	4303.60	0.25	0.57	657.34
EMM [49]	0.65	15.11	2445.93	0.28	0.59	271.68	EMM [49]	0.62	13.57	3002.12	0.30	0.57	491.85
SHI [50]	0.70	16.32	2350.22	0.33	0.56	246.16	SHI [50]	0.60	12.05	4459.79	0.29	0.49	432.90
TSJNet	0.72	14.93	2595.32	0.37	0.63	311.50	TSJNet	0.66	13.75	2992.80	0.34	0.55	415.43

3.3.3. Semantic Loss

Incorporating DeepLabV3+ [41] into our model significantly enhances the semantic information of the fusion results. The semantic loss can be expressed as:

$$\mathcal{L}_{\text{seg}} = -\frac{1}{PQ} \sum_{p=1}^P \sum_{q=1}^Q \log \left(\frac{\exp(\hat{y}_{c_{p,q},p,q})}{\sum_{j=1}^C \exp(\hat{y}_{j,p,q})} \right) \quad (12)$$

where $c_{p,q}$ represents the true class index at position (p, q) . $\hat{y}_{j,p,q}$ signifies the prediction of the model for class j at position (p, q) in logits.

4. UAV multi-scenario Benchmark

Conventional infrared and visible datasets, captured by ground-based fixed cameras with limited viewpoints, struggle to represent the real-world complexity and diversity. In contrast, the UMS dataset, leveraging aerial photography techniques, encompasses a broad spectrum of scenarios and target types, rendering it highly valuable for research.

Fig. 2 illustrates the UMS dataset captured using a DJI Matrice M30T UAV. This UAV is proficient in stable night and windy conditions for flight and photography. Its infrared camera operates within a spectral range of 8-14 μ m. The optical centers of the infrared and visible cameras are 3 cm apart. The captured visible and infrared images have



Figure 7: The proposed UMS dataset is visualized across six distinct scenarios: parking lots, parks, campuses, motorways, city street scenes, and residential areas.

resolutions of 4000×3000 and 1280×1024 , respectively. Additionally, the visible camera boasts a 21 mm focal length and a variable aperture (ranging from f/2.8 to f/4.2), enabling precise depth of field and brightness control. In contrast, the infrared sensor has a fixed aperture of f/1.0 and a 9.1 mm focal length, ensuring efficient IR spectral range capture and clear imaging. To construct this dataset, a series of flight paths were meticulously designed to facilitate data collection across diverse real-world scenarios in Foshan, China. All data collection activities were conducted in strict accordance with local regulations. The entire process was collaboratively completed by three researchers, who were respectively responsible for drone operation, simulating human targets during data acquisition, and organizing and integrating the collected data. The dataset construction spanned approximately two months.

To process the UMS dataset, visible images undergo initial cropping to match the size and view of infrared images. Subsequently, both image types align using the alignment algorithm of SuperFusion [47]. Each aligned image pair has a resolution of 640×512 and the dataset includes data captured from three distinct viewpoints: ground, drive, and flight. The UMS dataset comprises 346 image sets across six scenarios, including parking lot, park, campus, motorways, city street scenes, and residence, as depicted in Fig. 7. Additionally, we furnish labels for target detection and semantic segmentation, establishing a foundation for investigating image-fusion algorithms' impact on these tasks.

5. Experiment

5.1. Setup

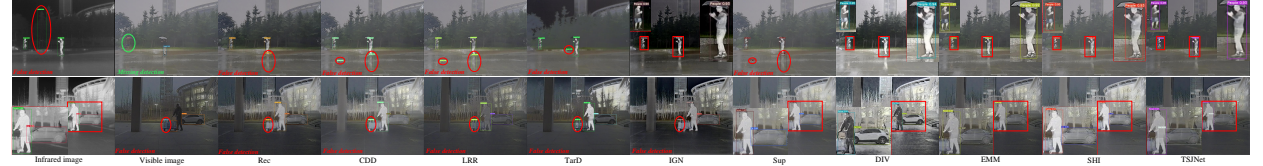


Figure 8: Detection results of different methods on M³FD dataset.

5.1.1. Experimental Detail

Experiments were conducted on a server equipped with two RTX 3090 GPUs. We trained using the original image size, avoiding chunking and resizing to preserve semantic information and avoid labeling failure. The training was carried out for 40 epochs with a batch size of 2, and the total training time was approximately 19.2 hours. The

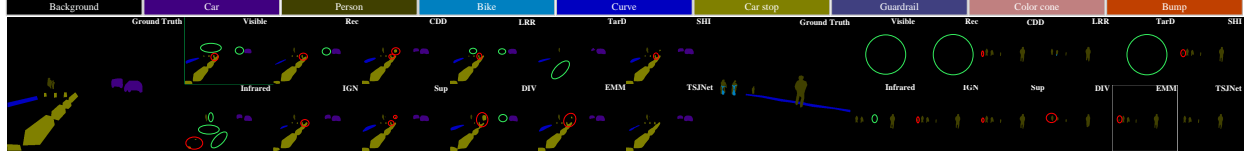


Figure 9: Segmentation results on the MSRS dataset, with missing and incorrect regions highlighted in green and red ovals.

Table 3: Comparison of TSJNet with seven methods for semantic segmentation on the MSRS and object detection on the M³FD. (The top three values are marked in red, green, and blue.)

Method	IoU (Dataset: MSRS [5])									AP@0.5 (Dataset: M ³ FD [4])							
	Background	Car	Person	Bike	Curve	Car Stop	Guardrail	Color Tone	Bump	mIoU	Peo	Car	Bus	Mot	Lam	Tru	mAP@.5
Visible	97.92	86.79	39.97	70.50	53.33	71.85	85.90	65.44	79.16	0.7232	0.803	0.912	0.946	0.841	0.667	0.890	0.843
Infrared	96.14	61.90	70.00	24.46	33.64	20.67	0.00	20.98	27.97	0.3953	0.777	0.733	0.597	0.113	0.519	0.611	0.558
ReC [46]	97.57	83.08	56.20	58.06	37.91	57.34	77.66	55.83	59.68	0.6481	0.803	0.912	0.946	0.841	0.667	0.890	0.843
CDD [11]	97.64	90.28	72.37	72.06	63.32	73.27	82.05	64.34	80.57	0.7732	0.832	0.916	0.953	0.844	0.705	0.882	0.855
) LRR [10]	98.31	88.85	67.21	69.56	52.12	71.51	81.07	63.93	77.63	0.7446	0.796	0.923	0.955	0.866	0.721	0.899	0.860
TarD [4]	97.52	82.12	55.17	63.56	38.83	63.94	58.58	53.15	45.89	0.6208	0.826	0.897	0.918	0.749	0.679	0.874	0.824
IGN [16]	98.46	89.48	74.01	70.76	57.69	73.62	83.59	64.24	72.96	0.7609	0.849	0.894	0.917	0.750	0.650	0.866	0.821
Sup [47]	96.43	88.24	73.21	72.22	62.77	73.20	82.25	65.18	80.15	0.7709	0.837	0.910	0.932	0.774	0.700	0.858	0.835
DIV [48]	98.05	87.38	64.63	67.02	50.63	69.43	78.37	61.47	44.38	0.6904	0.726	0.898	0.925	0.792	0.638	0.887	0.811
EMM [50]	98.58	90.00	72.92	71.10	64.38	74.48	84.11	65.68	74.32	0.7729	0.825	0.826	0.820	0.744	0.720	0.577	0.752
SHI [49]	98.52	89.54	72.87	71.55	63.69	73.26	84.76	65.44	74.58	0.7713	0.821	0.817	0.810	0.742	0.874	0.497	0.760
TSJNet	98.55	89.97	73.73	71.32	63.59	73.90	82.71	64.69	77.48	0.7733	0.818	0.918	0.956	0.868	0.704	0.893	0.860

Adam optimization function was employed with an initial learning rate of 0.001. When loss function stalled for three consecutive times, the learning rate was reduced by a factor of 0.1. For object detection and semantic segmentation, we utilized pre-trained Fast R-CNN models with ResNet-50 and FPN [42], along with a pre-trained DeepLabV3+ model using ResNet101 [41]. The three adjustable parameters α_1 , α_2 , and α_3 in Eq.9 are set as 0.1, 6, and 1, respectively.

5.1.2. Datasets, Metrics, and Compared methods

Datasets: Our model was trained on the MSRS dataset [5] (1035 pairs) and was subsequently tested on MSRS (361 pairs), M³FD [4] (300 pairs), RoadScene [22] (221 pairs), TNO [21] (129 pairs), LLVIP [23] (3463 pairs), and our constructed UMS (326 pairs). These datasets were synthetically generated to assess the generalization capability of our fusion network. Specially, the M³FD, RoadScene, LLVIP, and TNO datasets lack semantic segmentation labels or object detection labels, which is not conducive to conducting experiments on downstream tasks. Therefore, we provide these two kinds of labels for the four datasets with YOLO-v7 [51] and the Segment-anything model [52], which will be open-source in GitHub.

Metrics: structural similarity (SSIM), mean squared error (MSE), peak signal-to-noise ratio (PSNR), fidelity of visual information (VIF) [53], correlation coefficient (CC) [54], and Chen-Varshney metric (CV) [55]. These metrics were chosen to capture different aspects of image quality, including structural integrity (SSIM, PSNR), pixel-level accuracy (MSE), visual fidelity (VIF), correlation between predicted and source image values (CC), and overall perceptual similarity (CV), thus providing a well-rounded assessment of image quality.

Compared approaches: Nine SOTA approaches were compared with the TSJNet: Reconet (Rec) [46], CDDFuse (CDD) [11], LRRNet (LRR) [10], TarDal (TarD) [4], IGNNet (IGN) [16], SuperFusion (Sup) [47], DIVFusion (DIV) [48], EMMA (EMM) [50], and SHIP(SHI) [49].

5.2. Assessments of multi-modal image fusion

Subjective Comparisons. In Fig. 6, we present subjective outcomes for the MSRS, M³FD, RoadScene, LLVIP, TNO, and UMS datasets. The images fused by TSJNet outperform those fused by the other SOTA methods. Specifically, TSJNet dramatically highlights targets, especially in low-light or overexposed areas, effectively distinguishing foreground targets from the background. Additionally, TSJNet retains rich edge and texture information that may be obscured in low-light conditions, such as car door frames, car front center nets, car logos, soldiers, bike wheels, and the trees.

Objective Comparisons. Table 2 lists the mean scores of six metrics for the six datasets. In general, TSJNet demonstrates superior objective performance across all six datasets, particularly excelling in SSIM, CC, and MSE, validating the high resemblance of fused results to the source images. The high PSNR values and low MSE values collectively reflect the stability of TSJNet in handling images from various scenes. TSJNet’s emphasis on cross-modal feature extraction and preservation of edge details contributes to outstanding VIF values, indicating its high visual fidelity. Overall, the proposed method consistently extracts texture, brightness, and useful information from source images across different scenes while effectively capturing target information.

5.3. Downstream applications

5.3.1. Object detection

Setup, we performed object detection on M³FD dataset, employed detector YOLO-v7 [51], and evaluated the detection performance by the mean average precision (mAP) calculated at an intersection over union (IoU) of 0.5 metric (mAP@0.5). The training epoch, batch size, and initial learning rate were set to 300, 16, and 0.01, respectively.

Objective analysis. As shown in Table 3, the values of AP@0.5 and mAP@0.5 of the fusion results were higher than those of the unfused unimodal images. CDD, LRR, SHI and TSJNet exhibited good detection performances. Notably, the overall detection performance of TSJNet is 7.97% higher than the average level of compared methods.



Figure 10: Subjective ablation comparisons of the MDM, detection loss and segmentation loss.

Subjective Analysis. As shown in Fig. 8, the detection results of M³FD on images 04000 and 00275 are presented. The detection results of fused images, which incorporate complementary modal image features, generally outperform those of single-modal images. However, the impact of fusion performance on detection accuracy varies across different methods. In image 00275, ReC, CDD, LRR, TarD, and Sup mistakenly detect the reflection of a person in the rain as a real person. In image 04000, ReC, CDD, LRR, TarD, and IGN incorrectly classify a bucket as a person, while DIV exhibits low detection confidence. In contrast, the fusion results from TSJNet contain rich target features with high confidence, effectively avoiding these misclassifications.

5.3.2. Semantic segmentation

Setup, we used BiSeNet [56] to segment the semantic information of nine object classes of the MSRS dataset, *i.e.*, background, bump, color cone, guardrail, curve, bike, person, car stop, and car. The model’s effectiveness was assessed by IoU. The number of training epochs was set to 200, the batch size was eight, and the remaining parameters remained unchanged, as in the initial experiment [56].

Subjective analysis. Fig. 9 shows the segmentation results for “00939” and “00770” of MSRS. In the left example, the “yellow cones” cannot be segmented accurately by the compared methods, and ReC, LRR, and DIV cannot segment the distant cars. In the example on the right, ReC and TarD cannot segment any semantic information. CDD, IGN, Sup, DIV, EMM, and SHI have small errors in segmenting the “people” at the edge position. The better segmentation of “people” by TSJNet indicates that the fused images obtained by our model are better for semantic representation.

Objective analysis. Table 3 clearly demonstrates the segmentation superiority of TSJNet. The value of mIoU is the highest among the compared methods. Compared with its close competitors, CDD and Sup, TSJNet achieved

higher scores in many important categories, such as curves and car stops. Furthermore, TSJNet exceeds the average of other methods by 10.88% on the segmentation ability, which highlights the strong capabilities of our model in handling complex and detail-rich scenes.

5.4. Ablation studies

Ablation studies were conducted on the MSRS dataset. Table 4 summarizes the ablation results.

Ablation on the proposed MDM, MFM, and NAT. The MDM, MFM, and NAT play a vital role in perceiving continuous information in the image background as well as salient texture of targets. From Fig. 10, the image fused without the MDM has a limited ability for local brightness information extraction, *e.g.*, the tires of a car. Moreover, the absence of either the MFM or NAT modules leads to the loss of fine structural details.

Ablation on SA. SA aims to enhance the model’s adaptability and generalization ability to diverse scenarios. As illustrated in Fig. 10, although the removal of the SA module exhibits minimal effect on segmentation performance, it tends to cause false detections in the object detection results.

Ablation on detection and segmentation loss. To verify the effectiveness of detection and segmentation double losses, we removed them separately and jointly from TSJNet, leaving the other parts unchanged. As shown in Table 4, regardless of the type of loss removal, there is an overall downward trend in the metric values. As shown in Fig. 10, rich semantic and target information are extracted using dual loss. Thus, images fused with cross-modal information concurrently can achieve both robust detection and precise segmentation results. It means that the employment of detection and segmentation losses can establish mutually advantageous relationships between fusion and high-level tasks.

Table 4: Results of ablation experiments on MSRS.

Method	SSIM \uparrow	PSNR \uparrow	MSE \downarrow	CC \uparrow	CV \downarrow
w/o MDM	0.66	14.83	3731.88	0.54	560.46
w/o MFM	0.50	12.26	4218.04	0.46	451.98
w/o NAT	0.51	13.18	3384.58	0.55	473.36
w/o SA	0.52	13.41	3290.15	0.57	474.89
w/o \mathcal{L}_{Det}	0.55	14.86	2550.33	0.54	376.49
w/o \mathcal{L}_{Seg}	0.50	12.46	4167.93	0.60	464.51
w/o $\mathcal{L}_{\text{Det, Seg}}$	0.49	12.43	4246.27	0.51	363.24
TSJNet	0.69	18.13	1502.60	0.62	344.20

6. Computational complexity analysis

Table 5: Comparison of model complexity, computation, and inference time

Method	Parameters (M)	FLOPs (G)	Time (s)
ReC	0.008	1.518	0.021
CDD	1.186	29.213	0.363
LRR	0.197	3.022	0.191
TarD	0.297	91.138	0.084
IGN	53.969	107.938	0.014
Sup	1.962	76.630	0.070
DIV	4.400	722.540	3.000
EMM	1.520	17.724	0.065
SHI	0.548	401.510	5.980
TSJNet	45.070	2204.230	3.800

Table 5 compares the computational efficiency, FLOPs, and inference time of different methods. Although TSJNet does not demonstrate clear advantages in these aspects compared to other approaches, this is primarily due to its need

to simultaneously optimize three tasks: image fusion, segmentation, and detection. By trading off higher model complexity and computational overhead, TSJNet achieves notable performance improvements in image fusion and its downstream tasks.

7. Conclusion

This paper proposes a novel multi-modal image fusion network termed TSJNet. By integrating an autoencoder architecture with a Multi-Dimensional Feature Extraction Module (MDM), the proposed method effectively fuses multi-scale shared semantic features and salient modality-specific features. Furthermore, the joint optimization of fusion, segmentation, and detection losses significantly enhances the representation of cross-modal semantic and target information. Meanwhile, a spatial attention module introduced at the decoding stage improves the model's generalization capability across different data domains. In addition, we construct a UAV Multi-Scenario (UMS) benchmark dataset, which provides experimental support for the study and evaluation of multi-modal image fusion methods in real-world complex environments. Experimental results demonstrate that TSJNet can simultaneously enhance salient details and high-level semantic structures, thereby offering reliable support for downstream tasks such as object detection and semantic segmentation.

Looking ahead, we will focus on improving the TSJNet to be more streamlined and highly efficient to meet the demands of multisource heterogeneous data fusion in practical contexts such as autonomous driving and drone military operations.

8. Acknowledgment

This research was supported by the National Natural Science Foundation of China(No. 62201149), the Basic and Applied Basic Research of Guangdong Province(No. 2023A1515140077), the Natural Science Foundation of Guangdong Province (No.2024A1515011880), and the Research Fund of Guangdong-HongKong-Macao Joint Laboratory for Intelligent Micro-Nano Optoelectronic Technology (No. 2020B1212030010).

References

- [1] J. Liu, G. Wu, Z. Liu, D. Wang, Z. Jiang, L. Ma, W. Zhong, X. Fan, Infrared and visible image fusion: From data compatibility to task adaption, *IEEE Transactions on Pattern Analysis and Machine Intelligence* (2024).
- [2] Y. Sun, B. Cao, P. Zhu, Q. Hu, Dtfusion: A detection-driven infrared and visible image fusion network, in: *Proceedings of the 30th ACM International Conference on Multimedia*, 2022, pp. 4003–4011.
- [3] X. Li, Z. Gao, S. Liang, J. Zhang, R. Zhao, X. Liu, Csdfusion: Continuous knowledge trajectories for task-driven infrared and visible image fusion, *Knowledge-Based Systems* (2025) 115029.
- [4] J. Liu, X. Fan, Z. Huang, G. Wu, R. Liu, W. Zhong, Z. Luo, Target-aware dual adversarial learning and a multi-scenario multi-modality benchmark to fuse infrared and visible for object detection, in: *Proceedings of the IEEE/CVF Conference on Computer Vision and Pattern Recognition*, 2022, pp. 5802–5811.
- [5] L. Tang, J. Yuan, H. Zhang, X. Jiang, J. Ma, Piafusion: A progressive infrared and visible image fusion network based on illumination aware, *Information Fusion* 83 (2022) 79–92.
- [6] H. Li, J. Zhao, J. Li, Z. Yu, G. Lu, Feature dynamic alignment and refinement for infrared–visible image fusion: Translation robust fusion, *Information Fusion* 95 (2023) 26–41.
- [7] C. Lin, T. Liu, Z. Wang, B. Wang, Ctiufuse: A cnn-transformer-based iterative feature universal fusion algorithm for multimodal images, *Knowledge-Based Systems* (2025) 114313.
- [8] L. Tang, Y. Deng, X. Yi, Q. Yan, Y. Yuan, J. Ma, Drmf: Degradation-robust multi-modal image fusion via composable diffusion prior, in: *Proceedings of the 32nd ACM International Conference on Multimedia*, 2024, pp. 8546–8555.

[9] Y. Xu, X. Li, Y. Jie, H. Tan, Simultaneous tri-modal medical image fusion and super-resolution using conditional diffusion model, in: International Conference on Medical Image Computing and Computer-Assisted Intervention, Springer, 2024, pp. 635–645.

[10] H. Li, T. Xu, X.-J. Wu, J. Lu, J. Kittler, Lrrnet: A novel representation learning guided fusion network for infrared and visible images, *IEEE transactions on pattern analysis and machine intelligence* (2023).

[11] Z. Zhao, H. Bai, J. Zhang, Y. Zhang, S. Xu, Z. Lin, R. Timofte, L. Van Gool, Cddfuse: Correlation-driven dual-branch feature decomposition for multi-modality image fusion, in: Proceedings of the IEEE/CVF Conference on Computer Vision and Pattern Recognition, 2023, pp. 5906–5916.

[12] J. Zhang, L. Jiao, W. Ma, F. Liu, X. Liu, L. Li, P. Chen, S. Yang, Transformer based conditional gan for multimodal image fusion, *IEEE Transactions on Multimedia* (2023).

[13] Y. Jie, X. Li, T. Tan, L. Yang, M. Wang, Multi-modality image fusion using fuzzy set theory and compensation dictionary learning, *Optics & Laser Technology* 181 (2025) 112001.

[14] Y. Fan, W. Ran, K. Tan, Q. Liu, D. Yuan, X. Li, Y. Liu, D2fusion: Dual-domain feature decoupling for infrared and visible image fusion, *Knowledge-Based Systems* (2025) 114892.

[15] J. Yue, L. Fang, S. Xia, Y. Deng, J. Ma, Dif-fusion: Towards high color fidelity in infrared and visible image fusion with diffusion models, *arXiv preprint arXiv:2301.08072* (2023).

[16] J. Li, J. Chen, J. Liu, H. Ma, Learning a graph neural network with cross modality interaction for image fusion, in: Proceedings of the 31st ACM International Conference on Multimedia, 2023, pp. 4471–4479.

[17] X. Fan, X. Zhou, S. Liu, L. Sun, B. Xiao, Sdlfusion: A salient-aware differentiated learning network for infrared and visible image fusion, *Knowledge-Based Systems* (2025) 114836.

[18] X. Li, F. Zhou, H. Tan, W. Zhang, C. Zhao, Multimodal medical image fusion based on joint bilateral filter and local gradient energy, *Information Sciences* 569 (2021) 302–325.

[19] X. Li, X. Li, T. Ye, X. Cheng, W. Liu, H. Tan, Bridging the gap between multi-focus and multi-modal: a focused integration framework for multi-modal image fusion, in: Proceedings of the IEEE/CVF winter conference on applications of computer vision, 2024, pp. 1628–1637.

[20] W. Zhao, S. Xie, F. Zhao, Y. He, H. Lu, Metafusion: Infrared and visible image fusion via meta-feature embedding from object detection, in: Proceedings of the IEEE/CVF Conference on Computer Vision and Pattern Recognition, 2023, pp. 13955–13965.

[21] A. Toet, The tno multiband image data collection, *Data in brief* 15 (2017) 249–251.

[22] H. Xu, J. Ma, Z. Le, J. Jiang, X. Guo, Fusiondn: A unified densely connected network for image fusion, in: Proceedings of the AAAI conference on artificial intelligence, Vol. 34, 2020, pp. 12484–12491.

[23] X. Jia, C. Zhu, M. Li, W. Tang, W. Zhou, Llvip: A visible-infrared paired dataset for low-light vision, in: Proceedings of the IEEE/CVF international conference on computer vision, 2021, pp. 3496–3504.

[24] H. Li, X.-J. Wu, Crossfuse: A novel cross attention mechanism based infrared and visible image fusion approach, *Information Fusion* 103 (2024) 102147.

[25] X. Geng, L. Jiao, L. Li, X. Liu, F. Liu, S. Yang, Fast and effective: Progressive hierarchical fusion classification for remote sensing images, *IEEE Transactions on Multimedia* (2024).

[26] J. Liu, Z. Liu, G. Wu, L. Ma, R. Liu, W. Zhong, Z. Luo, X. Fan, Multi-interactive feature learning and a full-time multi-modality benchmark for image fusion and segmentation, in: Proceedings of the IEEE/CVF international conference on computer vision, 2023, pp. 8115–8124.

[27] J. Ma, H. Zhang, Z. Shao, P. Liang, H. Xu, Ganmcc: A generative adversarial network with multiclassification constraints for infrared and visible image fusion, *IEEE Transactions on Instrumentation and Measurement* 70 (2020) 1–14.

[28] X. Li, W. Liu, X. Li, F. Zhou, H. Li, F. Nie, All-weather multi-modality image fusion: Unified framework and 100k benchmark, *Information Fusion* (2026) 104130.

[29] W. Tang, F. He, Y. Liu, Itfuse: An interactive transformer for infrared and visible image fusion, *Pattern Recognition* 156 (2024) 110822.

[30] Z. Zhao, H. Bai, Y. Zhu, J. Zhang, S. Xu, Y. Zhang, K. Zhang, D. Meng, R. Timofte, L. Van Gool, Ddfm: denoising diffusion model for multi-modality image fusion, in: *Proceedings of the IEEE/CVF International Conference on Computer Vision*, 2023, pp. 8082–8093.

[31] B. Yang, Z. Jiang, D. Pan, H. Yu, G. Gui, W. Gui, Lfdt-fusion: a latent feature-guided diffusion transformer model for general image fusion, *Information Fusion* 113 (2025) 102639.

[32] L. Qu, S. Liu, M. Wang, Z. Song, Transmef: A transformer-based multi-exposure image fusion framework using self-supervised multi-task learning, in: *Proceedings of the AAAI conference on artificial intelligence*, Vol. 36, 2022, pp. 2126–2134.

[33] H. Li, X.-J. Wu, J. Kittler, Rfn-nest: An end-to-end residual fusion network for infrared and visible images, *Information Fusion* 73 (2021) 72–86.

[34] X. Li, X. Li, T. Tan, H. Li, T. Ye, Umcfuse: A unified multiple complex scenes infrared and visible image fusion framework, *IEEE Transactions on Image Processing* (2025).

[35] H. Zhang, H. Xu, Y. Xiao, X. Guo, J. Ma, Rethinking the image fusion: A fast unified image fusion network based on proportional maintenance of gradient and intensity, in: *Proceedings of the AAAI conference on artificial intelligence*, Vol. 34, 2020, pp. 12797–12804.

[36] Z. Liu, J. Liu, G. Wu, L. Ma, X. Fan, R. Liu, Bi-level dynamic learning for jointly multi-modality image fusion and beyond, *arXiv preprint arXiv:2305.06720* (2023).

[37] L. Tang, H. Zhang, H. Xu, J. Ma, Rethinking the necessity of image fusion in high-level vision tasks: A practical infrared and visible image fusion network based on progressive semantic injection and scene fidelity, *Information Fusion* (2023) 101870.

[38] H. Xu, J. Ma, J. Yuan, Z. Le, W. Liu, Rfnet: Unsupervised network for mutually reinforcing multi-modal image registration and fusion, in: *Proceedings of the IEEE/CVF conference on computer vision and pattern recognition*, 2022, pp. 19679–19688.

[39] D. Wang, J. Liu, X. Fan, R. Liu, Unsupervised misaligned infrared and visible image fusion via cross-modality image generation and registration, *arXiv preprint arXiv:2205.11876* (2022).

[40] H. Li, Z. Yang, Y. Zhang, W. Jia, Z. Yu, Y. Liu, Mulfs-cap: Multimodal fusion-supervised cross-modality alignment perception for unregistered infrared-visible image fusion, *IEEE Transactions on Pattern Analysis and Machine Intelligence* (2025).

[41] L.-C. Chen, G. Papandreou, F. Schroff, H. Adam, Rethinking atrous convolution for semantic image segmentation, *arXiv preprint arXiv:1706.05587* (2017).

[42] S. Ren, K. He, R. Girshick, J. Sun, Faster r-cnn: Towards real-time object detection with region proposal networks, *IEEE transactions on pattern analysis and machine intelligence* 39 (6) (2016) 1137–1149.

[43] H. Zhang, C. Wu, Z. Zhang, Y. Zhu, H. Lin, Z. Zhang, Y. Sun, T. He, J. Mueller, R. Manmatha, et al., Resnest: Split-attention networks, in: *Proceedings of the IEEE/CVF conference on computer vision and pattern recognition*, 2022, pp. 2736–2746.

[44] A. Hassani, S. Walton, J. Li, S. Li, H. Shi, Neighborhood attention transformer, in: Proceedings of the IEEE/CVF Conference on Computer Vision and Pattern Recognition, 2023, pp. 6185–6194.

[45] D. Chang, Y. Tong, R. Du, T. Hospedales, Y.-Z. Song, Z. Ma, An erudite fine-grained visual classification model, in: Proceedings of the IEEE/CVF Conference on Computer Vision and Pattern Recognition, 2023, pp. 7268–7277.

[46] Z. Huang, J. Liu, X. Fan, R. Liu, W. Zhong, Z. Luo, Reconet: Recurrent correction network for fast and efficient multi-modality image fusion, in: European Conference on Computer Vision, Springer, 2022, pp. 539–555.

[47] L. Tang, Y. Deng, Y. Ma, J. Huang, J. Ma, Superfusion: A versatile image registration and fusion network with semantic awareness, *IEEE/CAA Journal of Automatica Sinica* 9 (12) (2022) 2121–2137.

[48] L. Tang, X. Xiang, H. Zhang, M. Gong, J. Ma, Divfusion: Darkness-free infrared and visible image fusion, *Information Fusion* 91 (2023) 477–493.

[49] N. Zheng, M. Zhou, J. Huang, J. Hou, H. Li, Y. Xu, F. Zhao, Probing synergistic high-order interaction in infrared and visible image fusion, in: Proceedings of the IEEE/CVF Conference on Computer Vision and Pattern Recognition, 2024, pp. 26384–26395.

[50] Z. Zhao, H. Bai, J. Zhang, Y. Zhang, K. Zhang, S. Xu, D. Chen, R. Timofte, L. Van Gool, Equivariant multi-modality image fusion, in: Proceedings of the IEEE/CVF Conference on Computer Vision and Pattern Recognition, 2024, pp. 25912–25921.

[51] C.-Y. Wang, A. Bochkovskiy, H.-Y. M. Liao, Yolov7: Trainable bag-of-freebies sets new state-of-the-art for real-time object detectors, in: Proceedings of the IEEE/CVF Conference on Computer Vision and Pattern Recognition, 2023, pp. 7464–7475.

[52] A. Kirillov, E. Mintun, N. Ravi, H. Mao, C. Rolland, L. Gustafson, T. Xiao, S. Whitehead, A. C. Berg, W.-Y. Lo, et al., Segment anything, in: Proceedings of the IEEE/CVF International Conference on Computer Vision, 2023, pp. 4015–4026.

[53] H. R. Sheikh, A. C. Bovik, Image information and visual quality, *IEEE Transactions on image processing* 15 (2) (2006) 430–444.

[54] M. Deshmukh, U. Bhosale, et al., Image fusion and image quality assessment of fused images, *International Journal of Image Processing (IJIP)* 4 (5) (2010) 484.

[55] Z. Liu, E. Blasch, Z. Xue, J. Zhao, R. Laganiere, W. Wu, Objective assessment of multiresolution image fusion algorithms for context enhancement in night vision: a comparative study, *IEEE transactions on pattern analysis and machine intelligence* 34 (1) (2011) 94–109.

[56] C. Yu, J. Wang, C. Peng, C. Gao, G. Yu, N. Sang, Bisenet: Bilateral segmentation network for real-time semantic segmentation, in: Proceedings of the European conference on computer vision (ECCV), 2018, pp. 325–341.